Engineering Geology xxx (xxxx) 106371

Contents lists available at ScienceDirect

Engineering Geology

journal homepage: www.elsevier.com/locate/enggeo

Modelling the spatio-temporal evolution of a rainfall-induced retrogressive landslide in an unsaturated slope

Sabatino Cuomo [a,*], Angela Di Perna [a], Mario Martinelli [b,c]

[a] University of Salerno, Italy
[b] Deltares, Delft, Netherlands
[c] Technical University of Delft, Netherlands

ARTICLE INFO

Keywords:
Infiltration
Hydro-mechanical coupling
Numerical
LEM
FEM
MPM

ABSTRACT

Numerical modelling, particularly fully-coupled hydro-mechanical large-deformation models, greatly helps in properly simulating the complex failure and post-failure mechanisms of rainfall-induced landslides. The affected soils, in fact, evolve from none or small deformation rates to large deformation rates during the initiation stage and vice-versa during deposition, with relevant interactions between the solid skeleton and interstitial water. The Material Point Method (*MPM*) has the potential to reproduce entirely those complex processes. However, a comparison with standard tools (e.g. *FEM*: Finite Element Method, *LEM*: Limit Equilibrium Method) may guide in the optimal choice (or in the combined use) of the various modelling approaches. A framework is here proposed based on a multi-tool approach consisting in the combination of: a) *no-deformation LEM*, b) *small-deformation FEM*, c) *large-deformation MPM*. The *LEM* slope stability analyses are performed for a realistic assessment of the major slip surface(s) and to back-analyse uncertain slope parameters. The *FEM* stress-strain analyses assess the progressive failure, the onset of initial velocity and the later acceleration of the landslide body, until large deformations occur in the slope and numerical convergence of *FEM* is lost. The MPM analyses are used to reproduce the whole landslide process, from the initiation to propagation and final deposition. Such an integrated framework is tested for an international landslide benchmark (the 1995 *Fei Tsui Road* landslide in Hong Kong). The results achieved through the different approaches are discussed in relation to the wide scientific literature available for the general topics and the specific case study. The paper highlights that the fully-coupled hydro-mechanical large-deformation model properly reproduces the complex failure and post-failure mechanisms of rainfall-induced landslides. However, *no-deformation LEM* analyses and *small-deformation FEM* analyses allow a reasonable understanding of both the pre-failure stage and the failure mechanism. These more traditional tools are confirmed as indispensable tools in the engineering practice and research.

List of notations

a (−)	suction reduction parameter
$\mathbf{a}_L$ (m/s^2)	liquid acceleration
$\mathbf{a}_S$ (m/s^2)	solid acceleration
$\mathbf{b}$ (kPa)	body force vector
$c'(kPa)$	effective cohesion
$\mathbf{D}$ (kPa)	tangent stiffness matrix
$\mathrm{d}p_L$ (kPa)	increment of liquid pressure
$\mathrm{d}\boldsymbol{\sigma}'(kPa)$	increment of effective stress
E (kPa)	Young modulus of soil
FEM	Finite Element Method
F_{red} (−)	suction reduction factor
$\boldsymbol{f}_d$ (kPa)	drag force vector
$\boldsymbol{g}$ (m/s^2)	gravity vector
k (m^2)	intrinsic permeability
k_{rel} (−)	relative permeability factor
k_{sat} (m/s)	saturated hydraulic conductivity
$\mathbf{K}_L$ (kPa)	elastic bulk modulus of the liquid
LEM	Limit Equilibrium Method
MP	Material Point
MPM	Material Point Method
n (−)	porosity

* Corresponding author.
E-mail address: scuomo@unisa.it (S. Cuomo).

https://doi.org/10.1016/j.enggeo.2021.106371
Received 31 March 2021; Received in revised form 7 June 2021; Accepted 3 September 2021
0013-7952/

p_a (kPa)	air pressure
p_L (kPa)	liquid pressure
$p_{L,\ max}$ (kPa)	maximum liquid pressure
s (kPa)	matric suction
S_r $(-)$	degree of saturation
S_{res} $(-)$	residual degree of saturation
t (s)	time
v (m/s)	velocity of the mixture
V (m^3)	volume of the mixture
V_L (m^3)	liquid phase volume
V_S (m^3)	solid phase volume
$\mathbf{v}_L$ (m/s)	liquid velocity vector
$\mathbf{v}_S$ (m/s)	solid velocity vector
$\boldsymbol{w}$ (m/s)	Darcy's velocity vector
x (m)	horizontal Cartesian coordinate
y (m)	vertical Cartesian coordinate
α $(-)$	air entry value
β $(-)$	empirical coefficient
$\boldsymbol{\epsilon}$ $(-)$	cumulative strain vector
$\varepsilon_d(-)$	cumulative deviatoric strain
$\varepsilon_{d,\ thres}(-)$	cumulative deviatoric strain threshold
μ_L $(kPa \bullet s)$	liquid dynamic viscosity
υ $(-)$	Poisson's ratio
ρ_L (kg/m^3)	liquid density
ρ_m (kg/m^3)	density of the mixture
ρ_S (kg/m^3)	solid density
σ (kPa)	total stress tensor of the mixture
$\dot{\boldsymbol{\sigma}}$ (kPa/s)	Jaumann stress rate matrix
$\boldsymbol{\sigma}_n$ (kPa)	normal stress
φ' $(^\circ)$	internal friction angle
$\varphi_b'(^\circ)$	contact friction angle
ψ $(^\circ)$	dilatancy angle

1. Introduction

Slope failures are often associated with large deformations, which depend on slope geometry, soil type and triggering mechanisms (Cascini et al., 2013). Soil deformations may (*a*) concentrate along relatively thin shear bands or (*b*) occur within the whole landslide body. In the former case, a "localized" type of failure is observed, and it is challenging to reproduce the exact location of the shear bands with high soil shear strains inside, while most of the landslide body is almost undeformed. In the second case, again, a challenging task arises because the failure is "diffuse" inside the whole slope, generally with very large soil deformations. In both cases, there is the need to: *i*) smoothly reproduce the transition from "small" to "large" soil deformation when, and where, volumetric and shear strains develop, *ii*) accurately simulate soil large deformation during landslide propagation, and *iii*) capture the return from large to small deformation rates during deposition. The solid-like behaviour (for small deformation) and the fluid-like behaviour (for large deformation) of the involved soils are very different, and such a contrast is exacerbated in the so-called flow-like landslides, which predominantly affect poorly consolidated granular soils, weathered materials and loess all over the world (Cuomo, 2020).

Unsaturated soil condition is often a key factor in the pre-failure, failure and post-failure stages of rainfall-induced landslides. Before failure, the additional strength related to matric suction is fundamental for the equilibrium of granular soil slopes steeper than the effective friction angle. During the landslide pre-failure stage, soil suction gradually reduces because of rain infiltration. At failure or in the immediate post-failure stage, peculiar soil mechanical responses may even occur such as capillary collapse, i.e. a strong reduction of soil volume related to wetting (Yuan et al., 2019) or static liquefaction (Cascini et al., 2013). But also during landslide propagation, pore water pressures (positive or negative) undergo a spatio-temporal evolution depending on the accumulated deformation in the landslide body.

Most of the geotechnical analyses allow the separate modelling of the failure (Fernandez Merodo et al. 2004) and propagation stage of rainfall-induced landslides (Pastor et al., 2009). Regarding that, Cascini et al. (2010) highlight that the drained failure of shallow covers, caused by rainfall infiltration, can be adequately simulated through Limit Equilibrium Methods (*LEMs*) (Janbu 1954; Morgenstern and Price 1965). However, the most catastrophic landslides often involve complex interaction between the solid skeleton and the interstitial pore water. Hence, seepage analysis and stress-strain analysis should be jointly solved, and soil deformation properly taken into account. Several models based on the Finite Element Method (*FEM*) have been proposed for this aim. Hydro-mechanical coupled formulations have significantly developed over the years, based on the fundamental contribution of consolidation theory (Biot, 1941), and later generalizations (Pastor et al., 2014). However, soil deformations have been generally considered "small", that is reasonable when only pre-failure and failure are investigated. Globally, an enormous variety of applications of *LEM* and *FEM* approaches has been proposed for the last 30–40 years.

In more recent times, advanced numerical methods have focused on simulating soil large deformations. It is worth mentioning: (1) Discrete Element Method, namely *DEM*, (Li et al., 2019; Zhao et al., 2020); (2) Lagrangian particle-based methods such as Smooth Particle Hydrodynamics (*SPH*), Particle Finite Element Method (*PFEM*), *FEM* with Lagrangian Integration Points (*FEMLIP*), and Material Point Method (*MPM*) (Cuomo et al., 2013; Llano-Serna et al., 2016; Lee et al., 2019, Yerro et al., 2019); (3) coupled Eulerian-Lagrangian methods (Qiu et al. 2011; Chen et al., 2019).

MPM can model the coupled hydro-mechanical behaviour of a landslide process, and significant achievements are very recent. Some *MPM*-based studies investigate the failure of an unsaturated slope disregarding the infiltration process and imposing the critical phreatic surface (i.e. at slope failure) as initial condition for numerical modelling (Soga et al., 2016; Nguyen et al., 2021). Alternatively, short heavy rainfall is schematized as an assigned linear time decrease of suction along the ground surface (Yerro Colom, 2015, Yerro et al., 2016). In other studies (Wang et al., 2018; Lee et al., 2019; Lei et al., 2020) a zero pore-water pressure along the ground surface is assumed. In both the last two cases, a pore water pressure condition is imposed (e.g. ponding) at the ground surface boundary, and not a seepage inflow (e.g. rainfall intensity) as easily doable in more traditional approaches. The introduction of a flux boundary condition in the *MPM* context for rainfall infiltration modelling was firstly done by Bandara et al. (2016), using a fully-coupled hydro-mechanical $v - w$ formulation for saturated and unsaturated soils. This formulation is for instance employed by Liu et al. (2020) considering a constant water inflow (equal to the soil saturated hydraulic conductivity) applied to the ground surface for 1 h. Some other *MPM*-based studies focused on landslide propagation (Li et al., 2016; Conte et al., 2019; Yerro et al., 2019; Cuomo et al., 2021).

This paper provides a framework useful to perform different types of analyses, where: (1) different assumptions on soil deformations are done; (2) quantitative realistic solutions are achieved at each modelling level. The proposed framework is applied to an international landslide benchmark (the 1995 *Fei Tsui Road* landslide in Hong Kong), and the achieved results are discussed in relation to the wide literature available for the specific case study.

2. Methods

2.1. The framework proposed

The basic idea of this paper is to propose and test a framework for landslide modelling in unsaturated slopes, from initiation to final deposition.

The framework is based on a multi-tool approach, which aims to emphasize the combined use of standard and advanced computation models. *FEM* is one fundamental tool for simulating the pore water pressure regime in saturated and unsaturated conditions. Then, the slope evolution analysis can be pursued at three levels, under different hypotheses depending on the goals: a) no-deformation *LEM*, b) small-deformation *FEM*, c) large-deformation *MPM*. From a) to c) the modelling capability increases as well as the importance to well manage such advanced tools.

The novelty of such a framework relies on the capability of *MPM* to simulate from small- to large-deformation rates and vice-versa, as occurring during the landslide process, through a single mathematical approach.

A fundamental characteristic of the proposed framework is that the very different stress- and strain-rates during the initiation and propagation stages are tackled unitarily through *MPM*, provided that a proper soil mechanical model is adopted. The current discrepancy among the large varieties of small-strain soil constitutive models available and the more limited rheological models for propagation modelling also testifies the value of bridging such a gap.

The multi-scale timing is another feature of the proposed approach. There is, in fact, also a significant contrast in the times scales of the phenomena, which is afforded in this framework. For instance, the landslide propagation and deposition may last a few tens of seconds, or a few minutes at most (10^2 s). Whilst, a landslide triggering mechanism typically develops during rainfall and can last from few to tens of hours (10^5 s). The initial slope condition, for instance the initial water table height and the suction profile above the water table both depend on the many weeks or months before (10^7 s). In the proposed framework, the attention is posed on the combination of long- and short-term analyses (time scale from 10^5 to 1 s and less). For instance, one will be simulating the antecedent rainfall over 1–2 days (for instance, through *LEM* and *FEM*), and then looking for landslide transformation into a flow, propagation and deposition, all lasting some tens of seconds in total (through *MPM*). It is interesting noting that most of the current approaches alternatively allow the modelling of the long-term slope behaviour until a failure (time scale of 10^5 to 10^7 s) or solely focus on the propagation stage (10^2 s). Aimed to keep affordable the computational cost of an *MPM* modelling of the whole landslide process, a multi-resolution time schematization is adopted. A time step of 1 h and permeability expressed in m/h is used for hour-long simulation, when the slope is mostly undeformed and the acceleration of the solid skeleton are negligible. Then, a unit time of 1 s is used for the simulation of the landslide dynamics. For each of these two successive analyses the time step is automatically reduced if needed to ensure numerical stability.

The integrated use of three above-mentioned tools (*LEM*, *FEM*, *MPM*) is encouraged. Once their similarities and connections are outlined, then their results can be consistently compared. It will be shown, for instance, that the simpler *LEM* and *FEM* are sufficient to fully describe the landslide triggering, while *MPM* is necessary to cope with retrogressive failure. The three tools are hereafter presented from the most comprehensive formulation (*MPM*) to the most simplified one (*LEM*), presenting the various simplifications made.

2.2. Large-deformation material point method

MPM is an enhancement of *FEM*, being also well suited for large-deformation problems (Sulsky et al., 1994). A continuum body is schematized by a number of Lagrangian points (named Material Points), which carry all the physical properties and stress-strain values. The *MPs* can move through a background fixed mesh, which is used to solve the governing equations without storing any permanent information.

For saturated or unsaturated soils, the medium is here divided into two phases (solid and liquid) denoted by the subscripts of *S* and *L*, respectively. The subscript of *m* indicates the mixture. The interaction between the phases is tackled through the *two-phase single-point* formulation (Jassim et al. 2013; Ceccato et al., 2019). Only one set of material points is used for both the two phases. Solid and liquid acceleration fields ($\mathbf{a}_S - \mathbf{a}_L$ formulation) are the primary unknowns.

This formulation was mainly developed to model problems in saturated soil. However, more recently, it was also applied including the effects of partial saturation in the soil response (Wang et al., 2018, Ceccato et al., 2019, Martinelli et al., 2020). In this paper, the formulation summarized in Martinelli et al. (2020) is used. The main simplifications are: (*i*) the governing equations for the gas phase are neglected, (*ii*) the mass exchange of air and water between the liquid and gas phases are also neglected, (*iii*) air pressure is set to zero. Compared to more general three phases formulations (solid, water, air), for instance proposed by Yerro et al. (2016), Ceccato et al. (2019) outline that in many real cases of geohazards the differences between three phases and two phases formulations are negligible, and that the simplified formulation reduces significantly the computational cost.

The concept of Bishop (1954) effective stress is used to include the effect of partial saturation soil condition (Eq. (1)), where $s = -p_L$ is the matric suction, and $\boldsymbol{I}$ is the identity matrix.

$$\boldsymbol{\sigma}' = \boldsymbol{\sigma} - \mathrm{S_r} s \mathbf{I} \tag{1}$$

The relationship between soil degree of saturation (S_r), from unity to the residual degree of saturation (S_{res}), and soil matric suction is modelled through the van Genuchten (1980) equation as reported below, being α and β the function shape factors:

$$\mathrm{S}_r\left(p_L\right) = \mathrm{S}_{res} + \left(1 - \mathrm{S}_{res}\right)\left[1 + \left(\frac{p_L}{\alpha}\right)^{\frac{1}{1-\beta}}\right]^{-\beta} \tag{2}$$

Given the saturated permeability (k_{sat}), the current permeability in a partially saturated state is equal to the product of k_{sat} multiplied by the relative permeability (k_{rel}). The latter is expressed as a function of the degree of saturation, as proposed by Mualem (1976), ranging from 1.0 for a saturated soil down to lower values as the saturation degree diminishes (Eq. (3)).

$$k_{rel}\left(S_r\right) = \left(\frac{S_r - \mathrm{S}_{res}}{1 - \mathrm{S}_{res}}\right)^{0.5}\left[1 - \left(1 - \left(\frac{S_r - \mathrm{S}_{res}}{1 - \mathrm{S}_{res}}\right)^{\frac{1}{\beta}}\right)\right]^2 \tag{3}$$

The general form of soil stress-strain relationship is presented incrementally in Eq. (4), where $\mathbf{D}$ is the tangent matrix, $\mathrm{d}\boldsymbol{\varepsilon}$ is the strain increment vector. For large deformation, the Jaumann stress rate is adopted, which writes the soil time derivative of the Cauchy stress tensor.

$$\mathrm{d}\boldsymbol{\sigma}' = \mathbf{D} \bullet \mathrm{d}\boldsymbol{\varepsilon} \tag{4}$$

The dynamic behaviour of a partially saturated soil (Martinelli et al., 2020) is described under the following general assumptions: (*i*) incompressible solid grains, isothermal condition, and no mass exchange between solid and liquid, as not relevant for most of the landslides, (*ii*) smooth spatial distribution of porosity and degree of saturation in the soil, as a reasonable assumption in most of the engineering applications (Ceccato et al., 2019).

In such a fully-coupled hydro-mechanical approach, the motion of a partially saturated soil is described by the system of two momentum balance equations, using separate velocity fields ($\mathbf{v}_S$ and $\boldsymbol{v}_L$) for solid and liquid phases, as in the Eqs. (5) and (6), respectively.

$$(1-n)\,\rho_S \boldsymbol{a}_S = \nabla \bullet \left(\boldsymbol{\sigma} - nS_r p_L \boldsymbol{I}\right) + \left(\rho_m - nS_r \rho_L\right)\boldsymbol{b} + \mathbf{f}_d \tag{5}$$

$$\rho_L \boldsymbol{a}_L = \nabla p_L + \rho_L \boldsymbol{b} - \mathbf{f}_d \tag{6}$$

The drag force vector $\mathbf{f}_d$ (in Eqs. (5) and (6)) is calculated through the Eq. (7), where Darcy's law is used to model solid-liquid interaction forces.

$$\mathbf{f}_d = \frac{nS_r \mu_L}{k_{rel} k}\left(\mathbf{v}_L - \mathbf{v}_S\right) \tag{7}$$

The mass balance equation of the solid skeleton is used to update the volume and the porosity of each *MP* (Eq. (8)). The mass balance equation for the liquid reads as Eq. (9), under the assumption of a barotropic liquid phase, so that the time derivative of liquid density is only a function of the time derivative of pore-water pressure.

$$\frac{\partial n}{\partial t} = (1-n)\,\nabla \bullet \boldsymbol{v}_S \tag{8}$$

$$\frac{\partial p_L}{\partial t} = \frac{K_L}{\left(1 - \frac{K_L}{S_r}\frac{\partial S_r}{\partial s}\right)}\left[\frac{(1-n)}{n}\nabla \bullet \boldsymbol{v}_S + \nabla \bullet \boldsymbol{v}_L\right] \tag{9}$$

Two different boundary conditions can be specified at ground level: (a) “ponding”, i.e. pore water pressure is set equal to zero, so that the infiltration flow is calculated from Eqs. (5)-(6), or (b) “infiltration”, with a user-specified inward seepage flow, with the pore water pressures computed at the boundary. True velocity fields for both liquid and solid are used in this numerical algorithm (Martinelli et al., 2020), instead of Darcy's seepage velocity, used in other implementations (Bandara et al., 2016).

The maximum liquid pressure ($p_{L,\,max}$) is initially assumed equal to water cavitation pressure (100 kPa), which is reasonable for coarse-grained soils. Then, additional to the equation proposed by Lee et al. (2019), the maximum liquid pressure is reduced as the cumulative deviatoric strains increase ($F_{red} \bullet p_{L,\,max}$). The reduction factor F_{red} that multiplies the maximum suction ($p_{L,\,max}$) is reported in Eq. (10), where ε_d is the cumulative deviatoric strain, $\varepsilon_{d,\,thres}$ is the deviatoric strain where the suction vanishes and a is a parameter controlling the trend of suction reduction. The rationale of such a hypothesis relies on theoretical explanations and experimental evidence demonstrating the reduction of bonding capillary forces with the increasing distances of soil grains (Scholtès et al., 2009; Gras et al., 2013; Zhao et al., 2019). For instance, during the slope instability evolution, the shearing among the soil grains may lead to the breakage of water menisci. For this reason, soil suction here is decreased with increasing deviatoric strains and vanishes therefore at soil large-deformations.

$$F_{red} = 1 - \left(\frac{\varepsilon_d}{\varepsilon_{d,thres}}\right)^a \tag{10}$$

2.3. Small-deformation finite element method

An alternative landslide modelling approach is based on *FEM*, the most popular numerical method in geotechnical engineering and engineering geology. The basic equations for soil static deformation are formulated within the framework of continuum mechanics, to obtain stress-strain states respectful to gravity and external loads, and compatible with hydraulic boundary conditions.

The weak form of the governing equations and the final system of equations solved at the nodes of the computational mesh can be identical in *FEM* and *MPM*. This applies also to the soil hydraulic and shear strength functions used in *FEM* and *MPM*.

An important difference is how the numerical integrations are performed over the element volume. *FEM* integration uses Gaussian quadrature, while *MPM* calculation is based on material points. However, the most distinguishing feature is that standard *FEM* formulations refer to the original undeformed geometry of soil. Thus, the method is not well suited for large-deformation simulations. This inconvenience can be mitigated using the updated-Lagrangian formulation, where the problem is solved at the deformed soil geometry. However, for very large displacements experienced by many landslides such approach cannot find a solution as it suffers from extreme mesh distortion.

In this paper, the *FEM* solves a quasi-static set of balance equations, where the inertia terms are neglected. The balance equations are solved in terms of nodal displacements of the soil-water mixture and the liquid pore pressure, as follows:

$$\boldsymbol{K}d\boldsymbol{u} + \boldsymbol{Q}d\boldsymbol{p_L} = d\boldsymbol{f} \tag{11}$$

where $\boldsymbol{K}$ is the stiffness matrix, $\boldsymbol{Q}$ is the coupling matrix and $d\boldsymbol{f}$ is the incremental load vector of external forces.

The flow problem is written as follows:

$$-\boldsymbol{H}\boldsymbol{p_w} + \boldsymbol{Q}^T\frac{d\boldsymbol{u}}{dt} - S\frac{d\boldsymbol{p_L}}{dt} = \boldsymbol{q} \tag{12}$$

where $\boldsymbol{H}$, S and $\boldsymbol{q}$ are the permeability matrix, the compressibility matrix and the prescribed boundary conditions.

2.4. No-deformation limit equilibrium method

A even simpler uncoupled hydro-mechanical model is obtained if (*i*) water compressibility is assumed negligible and (*ii*) soil deformation rates are neglected. Eqs. (9) and (12) reduce to the well-known equation of Richards (1931) from which pore-water pressures can be computed, given the initial and boundary conditions. A time series of pore water pressure is obtained while the solid skeleton of soil is considered undeformed. From those known pore-water pressures, the slope Factor of Safety (*FS*) is computed, defined as the ratio of the shear strength of soil to the minimum shear strength required for equilibrium (Bishop, 1955). As the main advantage, the *LEM* approach only requires soil unit weight and shear strength as input data. For each potential slip surface, the soil mass is divided into vertical slices, and the problem reduces to the static equilibrium of a series of interacting rigid bodies. The problem is ill-posed and different hypotheses have been formulated to represent the internal forces, so that many *LEMs* are available in practice (Janbu, 1954; Bishop, 1955; Morgenstern and Price 1965; among others).

LEM-based models are applied to investigate the response of slope until failure. The effects of the hydrological variables (i.e., rainfall, infiltration) are evaluated in terms of changes in pore-water pressure and *FS*. However, soil deformation, deformation rates, and tempo-spatial evolution of soil deformation or shear strength locally mobilized into the slope are not assessed. Thus, serious limitations arise for *LEM* application to complex slope evolution mechanisms such as liquefaction, progressive failure, or retrogressive landslides.

3. Case study

The Fei Tsui Road landslide (Fig. 1) occurred in the Chai Wan District of Hong Kong, after the heavy rain of 12th and 13th August 1995 (Fig. 2). A cumulative rainfall of 374 mm was recorded in the last 12 h before failure (maximum intensity of 60 mm/h), combined to the highest rainfall amount recorded on the site for a storm longer than a week (943 mm in 15 days before failure). The landslide took place in two stages: the first failure occurred at about 00:55 on 13th August 1995 in the superficial part of the slope, involving some tens of cubic meters; about 20 min later, a large failure moved down about 14,000 m^3 of weathered volcanic rock. The debris travelled 70 m, invaded the Fei

Fig. 1. Landslide overview (modified from Ho and Lau, 2010).

Tsui Road, which is beneath the cut-slope, entered a playground and accumulated for about 6 m at a corner of a Church (Fig. 1). Landslide propagation also included moderate lateral spreading, so that it will be interesting to study the slope evolution in the main cross-section (in plane strain condition Fig. 3a) and also to analyse the landslide following the radial pattern of the unstable material (in axisymmetric condition, Fig. 3b). The maximum width and the average depth of the debris deposit were 90 m and 15 m, respectively (Fig. 4).

The first technical investigation was carried out by the Geotechnical Engineering Office (GEO) of Hong Kong, and described in the report No. 188 (Knill, 1996). It was ascertained that before the landslide, there was a densely vegetated cut-slope with a maximum height of 27 m and an overall inclination of 60° towards the North. The lower part of the slope (up to 8 m high from the ground) was constituted by exposed rock, grading from fresh to slightly decomposed volcanic rock. Above this material, kaolinite-rich layer (0.6 m in thickness) and moderately to completely decomposed tuff were arranged as shown in Fig. 4 (modified from Knill, 1996 and Kirk et al., 1997), in which the materials are also associated with their degrees of weathering (GCO, 1988).

The sliding surface of the landslide followed the kaolinitic layer only in the lower part, whereas such a layer is beneath the slip surface in the upper part of the slope (Fig. 4). From the field evidence, the lowest part of the cut-slope (composed by moderately to slightly decomposed tuff) did not form part of the landslide.

The geotechnical properties of the landslide materials were available from the above mentioned GEO report n°188 (Knill, 1996), which outlines the results of several laboratory tests including particle size distribution, Atterberg limits, oedometer, triaxial compression and direct shear tests.

A wide literature is available for this specific case study. The first slope stability analysis was performed through *LEM* by Knill (1996) for the diagnosis of the landslide mechanism. At that time, the unsaturated soil features were not considered, although important insights were ob-

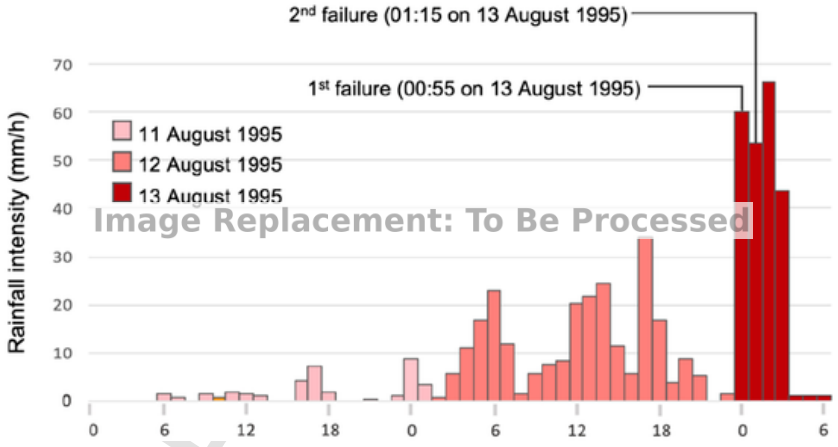

Fig. 2. Hourly rainfall intensity in the 2 days before failure (modified from Knill, 1996).

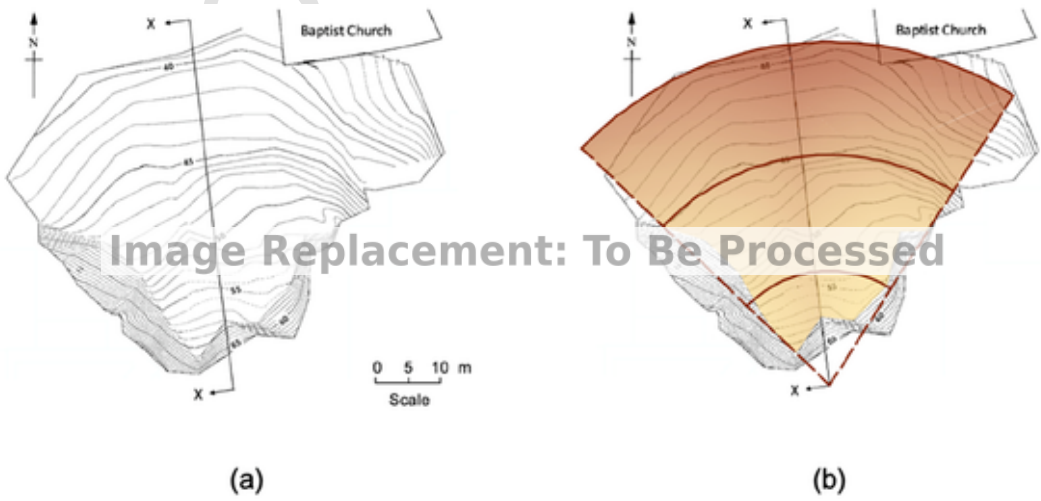

Fig. 3. Plan view of final landslide deposition: (a) contour lines and (b) radial pattern of the debris.

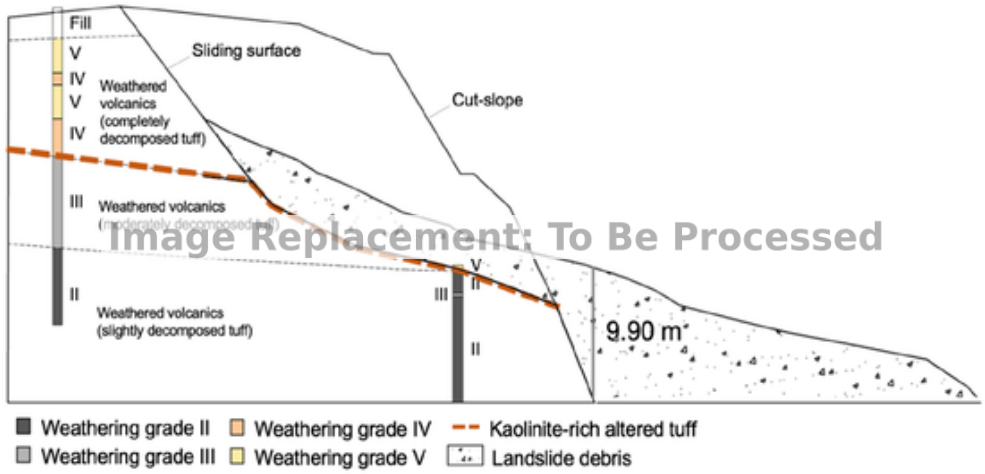

Fig. 4. Stratigraphic profile of the cut-slope (section X-X of Fig. 3).

tained: (*i*) a shear strength (φ') at failure of the altered tuff layer likely in the range of 26.5°–31.5°, (*ii*) a perched water table at failure from 1 m up to 4 m above such layer. The only *FEM*-based modelling of landslide triggering stage is that proposed by Cuomo et al. (2020), which highlights a potential progressive failure occurred into the slope. Indeed, the rest of the literature focuses on landslide propagation, through *SPH* modelling (Chen and Lee, 2000; Wang and Sassa, 2010; Sanchez et al., 2013; Pastor et al., 2014; Calvello et al., 2017; Cuomo et al., 2017; Koo et al., 2017) or MPM modelling (Ghasemi, 2019; Lee et al., 2019). The best estimates are achieved with the assumption of two basal friction angles, precisely 22°–26° along the kaolinitic layer and 30°–35° on the urbanized area. A recent *MPM*-based contribution (Liu et al., 2020) considers the unsaturated soil condition, and simulates the landslide triggering and propagation. However, some major simplifications are still included: (*i*) behind the scarp of landslide, a cohesion of some hundreds of kPa is assumed, i.e. practically undeformable, so that the computed soil deformations are constrained along a given soil contact layer, (*ii*) a water inflow equal to soil saturated permeability (k_{sat}) is assigned to the ground surface. However, in unsaturated slopes, soil suction creates the chance for infiltration rates higher than k_{sat} at the beginning of rainfall, and then equal or lower than k_{sat} as the time goes ahead, (Cuomo and Della Sala, 2013; among others). This simplification also prevents the estimate of the initial soil suction in the slope. Consequently, a quick landslide motion (about 160 s) is reproduced and either the long-term infiltration process or the real spatio-temporal evolution of the landslide is not captured.

In the present paper, the measured 26 hourly rainfall intensity values are used as input of the three types of approaches mentioned before, among which the *large-deformation MPM* modelling. The achievement of a "perfect" back-analysis is far from the goal of this paper, which instead discusses different approaches for a well-documented case study, whose input data have been worldwide available and used for testing alternative methods.

4. No-deformation LEM analyses

This section aims to assess the initial soil suction (i.e. before critical rainfall), which surely played a role in slope instability and landslide evolution. Firstly, pore-water pressures are modelled to compute the changes induced by the heavy rainfall (24 h long) that preceded the landslide event. The groundwater modelling is performed through the commercial FEM code Seep/W (GeoStudio Manual, 2012), with a mesh of 2240 triangular elements, 1 m sized on average (Fig. 5). The saturated hydraulic conductivity value is equal to $5{\cdot}10^{-5}$ m/s, and the soil water retention curve and conductivity function are taken from Ghasemi (2019). The geotechnical parameters of the completely decomposed tuff (CDT) are taken from Ng et al. (2011). A flux boundary condition equal to the hourly rainfall intensities (Fig. 2) is assumed at the ground surface. As initial condition, the unknown suction distribution is assumed homogeneous all over the slope section and varied among different scenarios (from 40 to 60 kPa, with a 5 kPa interval).

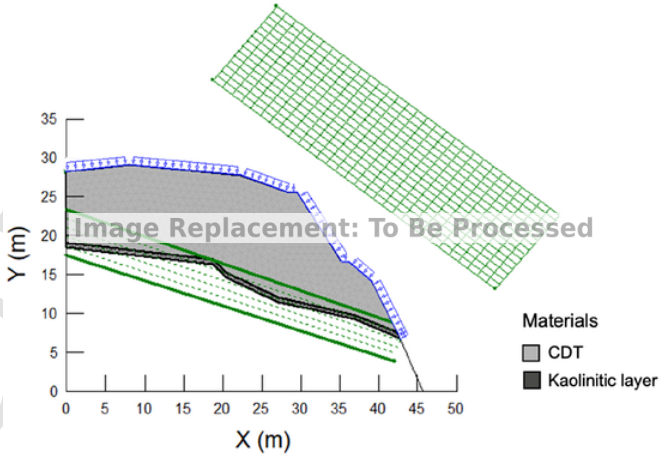

Fig. 5. Computational FEM mesh used for the seepage analysis with the indication of the soils, the rainfall boundary condition, as well as the grid of points and the radius lines used to define more than 2000 slip surfaces.

Independent on the initial suction assumed, the seepage analysis clearly outlines that: (*i*) a perched water table arises above the kaolin-rich layer, (*ii*) above the water table, soil suction is progressively lowered over the time, (*iii*) in agreement with the literature (Knill, 1996), the water table depth is in the range 1.5–4.5 m above the kaolinitic layer, at the time of the deepest slope failure (i.e. t = 25 h).

Those pore water pressures are used as input data for the slope stability analyses to assess the spatio-temporal evolution (during rainfall infiltration) of the Factor of Safety (*FS*) along superficial or deep slip surfaces.

The Morgenstern-Price (1965) method, and the commercial code Slope/W (GeoStudio Manual, 2012) are used. A rigid perfectly-plastic constitutive model is adopted, considering the extended Mohr-Coulomb failure criterion proposed by Fredlund et al. (1978) for the unsaturated soils. More than 2000 pseudo-circular slip surfaces are specified through a grid of centres and a range of radius (Fig. 5). Estimates of the internal friction angle of the kaolinitic layer (22–29°) and the effective cohesion of the completely decomposed tuff (0–10 kPa) are taken from the literature. All the used soil parameters are listed in Table 1.

Table 1
Material properties used as input for the LEM analysis.

Materials	ρ_m (kg/m^3)	k_{sat} (m/s)	E (MPa)	ν (–)	c' (kPa)	φ' (°)	ψ (°)	α (kPa)	β (–)	S_{res} (–)
CDT	1937	5 10^{-5}	10	0.3	5	35	0	64	0.47	0.275
Kaolinitic layer	1937	10^{-7}	10	0.3	0	29	0	–	–	–

The spatial distribution of the *FS* computed for some reference time lapses is reported in Fig. 6. It is noted that the LEM analyses well reproduce the observed slope instability only assuming an initial suction of 50 kPa. In this case, the slope is simulated as initially stable (Fig. 6a). It remains stable ($FS > 1$) during the first 12 h of rain (Fig. 6b), with $FS > 1.1$ at any potential slip surface, while the perched water table is rising. After about 24 h, *FS* drops below unity along a shallow slip surface (Fig. 6c). After 1 h more, a deeper slip surface reaches a similar unstable condition (Fig. 6d). For several slip surfaces, *FS* progressively reduces over the time, for the shallow surfaces first and then for the deep ones. This slope evolution resembles the retrogressive failure mechanism reported by the eyewitnesses.

It is also noted that the time-trend of *FS* is quite different for the shallow (Fig. 7a) and deep slip surfaces (Fig. 7b). For the shallow slip surfaces, *FS* rapidly decreases during rainfall infiltration, *FS* drops when the perched water table has formed at the base of the slope. The deep slip surfaces encounter a slower reduction of the factor of safety over the time.

A satisfactory agreement with field evidence is globally achieved. (*i*) For both the shallow and deep slip surfaces, *FS* diminishes below unity approximately at the time observed in the field for the two failures. (*ii*) The depth of the critical water table falls in the range reported in the literature. However, more sophisticated analyses are conducted to better understand the slope evolution from the occurrence of the shallow landslide until the deep failure.

5. Small-deformation FEM analyses

Hydro-mechanical coupled stress-strain FEM analyses are carried out using the commercial code Plaxis 2D (Plaxis 2D, 2018). The computational mesh is made of 6-noded triangular elements 1 m large, similar to the uncoupled seepage analysis. The updated mesh Lagrangian formulation of McMeeking and Rice (1974) is used. The materials included in the analysis are the completely decomposed tuff and the kaolinitic layer (schematized as a contact layer). The input parameters are the same as Table 1. The bottom of the computational domain is assumed as fully fixed (in both X- and Y-directions) (Fig. 8).

After computing the initial equilibrium geostatic stresses, a fully-coupled flow-deformation analysis is performed to simulate rainfall infiltration, with the consequent decrease in soil suction and rise of the perched water table. A fully implicit integration scheme is used, which allows large time steps and fast computation (Haxaire et al., 2011; Plaxis 2D, 2018). The analyses are carried out both in plane-strain and axisymmetric conditions (Fig. 9). The time-trend of displacement is computed in 5 control points located at the toe of the slope (Fig. 8) to compare the numerical results with the observed occurrence time. The failure time is deducted from any asymptotic-like time-trend of the computed displacements.

In all the cases, a slope failure is simulated at the lowest part of the slope (point B). Far from here, the displacements are smaller or negligible (points D and E). This is consistent with the field evidence of a retrogressive landslide. The initial suction leads to slightly different failure scenarios. For a lower initial suction (e.g. 50 kPa) the displacements are more differentiated inside the slope and the displacement rates are lower (Fig. 9) compared to a higher initial suction (e.g. 60 kPa). The simulated failure time is shorter for an initial suction of 50 kPa than for 60 kPa, especially in plane-strain condition. This confirms that the initial suction in the slope must be carefully considered in the slope stability analysis. In the axisymmetric simulations, the failure is reached later, obtaining a good correspondence with the observations for both an initial suction 50 and 60 kPa (Fig. 9).The shape of the shallow slip surface is given by the spatial distribution of the simulated plastic strains: (*i*) the results are similar in plane-strain (Fig. 10a) and axisymmetric (Fig. 10b) conditions, (*ii*) however, in the first case the slope failure is reached for an higher water table.

As a main limitation, the second and deeper failure is not simulated because the analysis stops (lack of numerical convergence) once the first small failure occurs. A large-deformation analysis (e.g. *MPM*-based) may overcome such limitations.

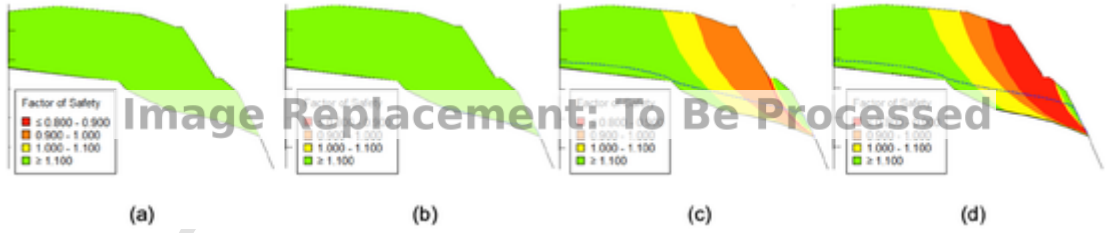

Fig. 6. Factor of safety spatial distribution for $s_0 = 50$ kPa: (a) $t = 0$; (b) $t = 12$ h; (c) $t = 24$ h and (d) $t = 25$ h.

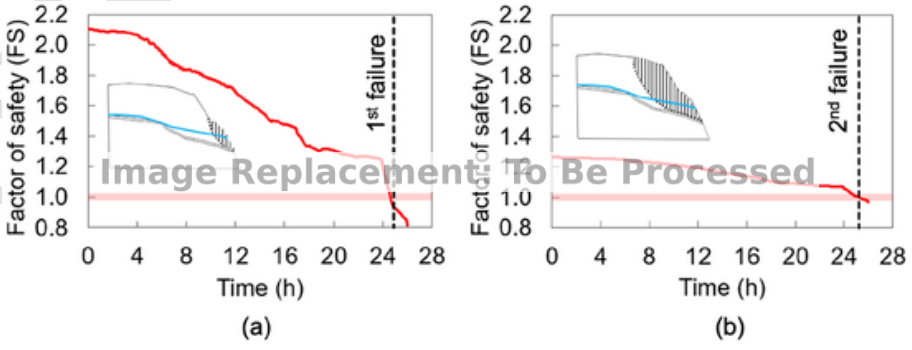

Fig. 7. Factor of safety changing in time for $s_0 = 50$ kPa: along (a) shallow and (b) deep slip surface.

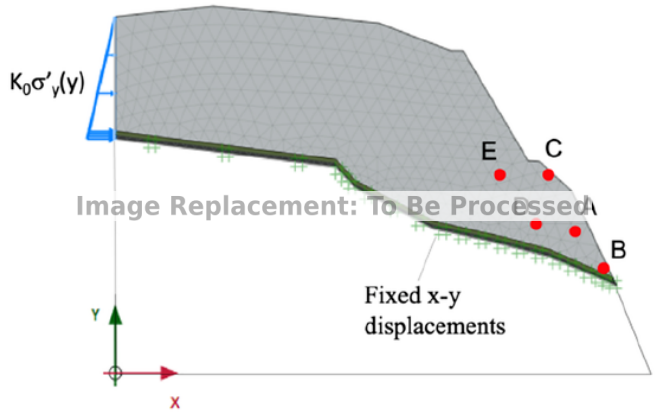

Fig. 8. FEM computational domain, with the element mesh, boundary constraints and monitored points.

6. Large-deformation MPM modelling

6.1. Parametric analysis

A large-deformation *MPM* analysis is conducted to simulate the pre-failure, failure and post-failure landslide stages through a unified mechanical model. One issue for the combined simulation of rainfall infiltration and slope failure mechanisms is related to the different time scales during the landslide process (Fig. 11a): *a*) the pre-failure stage (about 24 h), for which rainfall infiltration is the main issue to be tackled, the slope is stable and soil deformations are very small (from t_0 and t_{24}), *b*) the instability evolution, which includes the two failures (delayed of about 20 min) and *c*) the propagation and final deposition of the debris during few tens of seconds (from t_{24} to t_f). In the first stage (*a*) the time interval is assumed equal to 1 h, while the slope instability stage (*b*-*c*) is discretized in seconds. The computational *MPM* scheme is given in Fig. 11b. The upper Completely Decomposed Tuff (*CDT*) is included in the numerical analyses, and the lower kaolinite-rich layer is schematized as a contact surface, where a frictional contact algorithm is implemented. Another contact surface is considered between the urbanized zone and the landslide moving mass. The stress-strain response of the completely decomposed tuff is modelled as an elasto-plastic material with Mohr-Coulomb failure criterion. The soil unsaturated material is tackled through the two-phase single-point formulation, while the

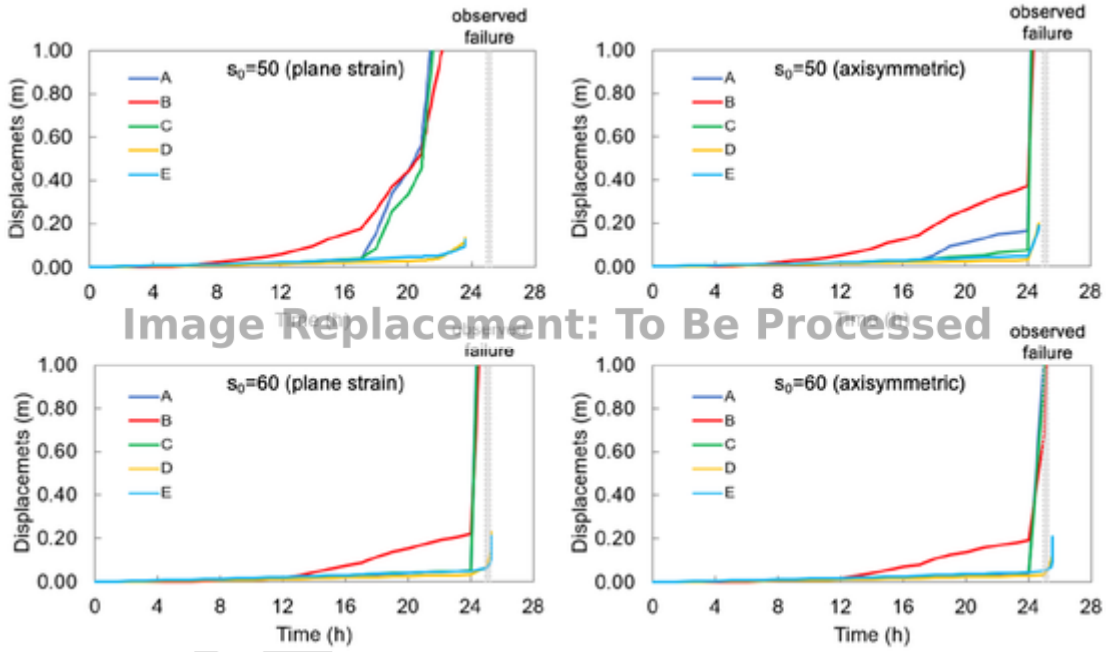

Fig. 9. Trend of displacements over time for two different initial suction values considering plane strain or axisymmetric schematization.

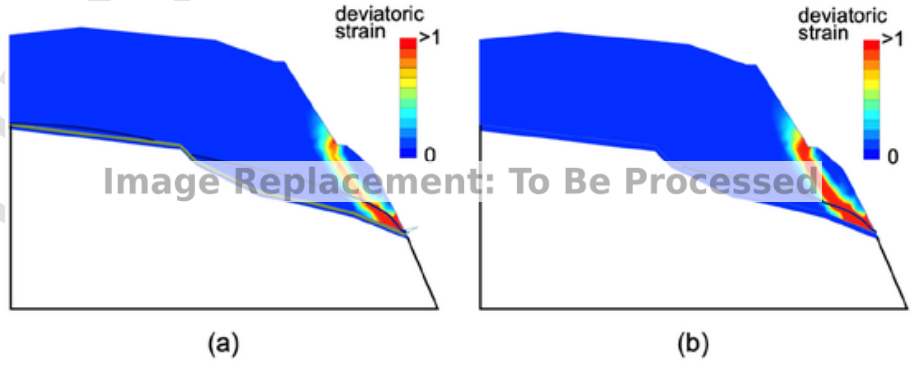

Fig. 10. Plastic deviatoric strain distribution at failure for s_0 = 50 kPa: (a) plane strain; (b) axisymmetric.

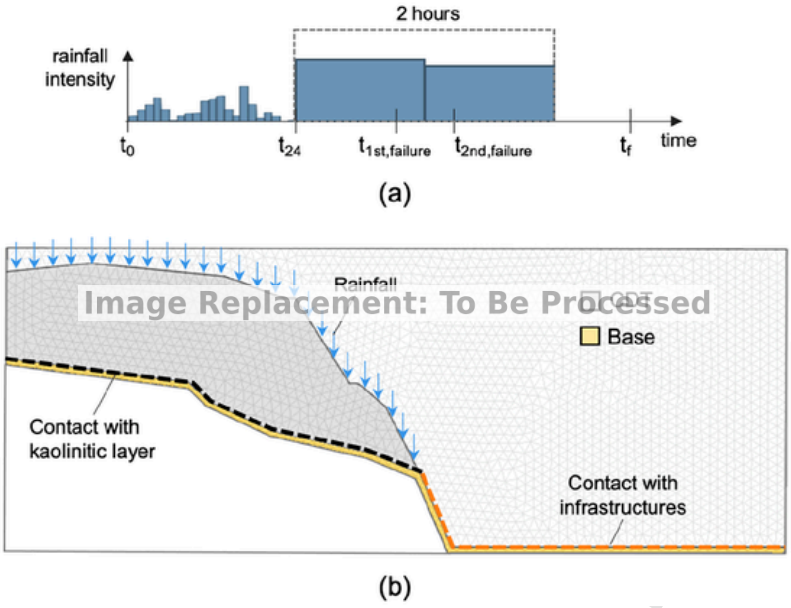

Fig. 11. (a) Simulations stages: infiltration (t_0-t_{24}) and propagation (t_{24}-t_f); (b) domain schematization including soil materials and contact surfaces.

one-phase single-point formulation is applied for the contact surfaces. The background calculation mesh is composed of 6753 triangular 3-noded elements, with an overall size of about 1 m assigned to the whole domain, and local refinements of the mesh. The rainfall input is the hyetograph of Fig. 1 and the initial suction value at the beginning of the rain is set as constant along the depth as done in the previous *FEM* analyses.

A parametric analysis is conducted by changing the input parameters which may affect more the landslide mechanisms: (*i*) the initial soil suction (s_0), (*ii*) the basal friction contact along the kaolinitic layer (φ'_{ka}*aolin*) and (*iii*) the exponent *a of* Eq. (10), which controls the trend of suction reduction, (*iv*) the contact friction along the Fei Tsui Road (φ'_b)to well reproduce the debris deposit. Both plane-strain and axisymmetric conditions are considered to point out the effects of lateral deformations. A recent version of the Anura3D code, developed by Deltares (Martinelli et al., 2020), is used to perform the *MPM* simulations. The goal is to achieve the closest correspondence with the field evidence in terms of occurrence time of the two failures, shape of the sliding surface and final configuration of the debris deposition.

Some selected results are reported in Tables 2 and 3 for the plane-strain and the axisymmetric simulations, respectively, and two Kiviat diagrams are also used (Fig. 12).

Table 2
Input and output of plane strain simulations.

ID	INPUT				OUTPUT		
	s_0 (kPa)	tan(φ_{kaolin})	tan(φ_{kaolin})/tan(φ'_b)	*a*	1st failure (h)	2nd failure (h)	run-out (m)
PS1	50	0.55	1.00	-∞	24.97	25.42	55
PS2	55	0.55	0.75	5	25.25	25.92	72
PS3	50	0.4	1.00	-∞	20.00	20.00	63
PS4	50	0.55	0.75	5	17.50	18.25	80
PS5	52.5	0.55	1.00	1	24.44	24.89	83

Table 3
Input and output of axisymmetric simulations.

ID	INPUT				OUTPUT		
	s_0 (kPa)	tan(φ_{kaolin})	tan(φ_{kaolin})/tan(φ'_b)	*a*	1st failure (h)	2nd failure (h)	run-out (m)
A1	50	0.55	0.75	1	24.63	25.17	78
A2	50	0.55	0.50	5	24.56	24.75	83
A3	52.5	0.55	0.75	5	24.75	25.03	71
A4	50	0.55	0.75	5	24.56	24.92	74
A5	55	0.55	0.75	5	25.42	25.72	77

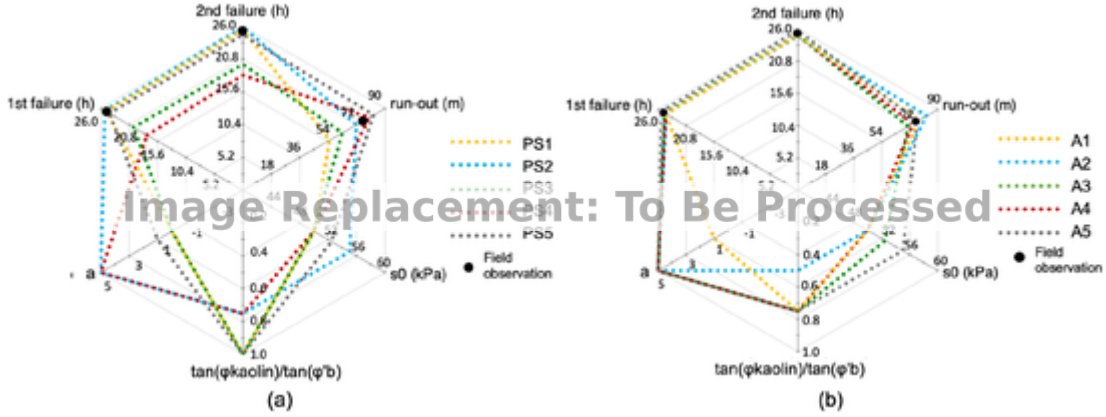

Fig. 12. Comparison of the numerical results with the field evidence as function of the input data:
(a) plane strain (PS1-PS5) and (b) axisymmetric simulations (A1-A5).

Table 4
CDT properties used as input for the MPM analysis.

ρ_S (kg/m^3)	n (–)	k_{sat} (m/s)	E (MPa)	ν (–)	c' (kPa)	φ' (°)	ψ (°)	ρ_L (kg/m^3)	K_L (MPa)	μ_L (Pas)	α (kPa)	β (–)	S_{res} (–)	$e_{d,\ thres}$ (–)	a (–)
2650	0.4	5×10^{-5}	10	0.3	5	35	0	1000	100	10^{-3}	64	0.47	0.275	1	1

The difference between the plane strain and the axisymmetric conditions is highlighted by the simulations named PS4 (plane strain) and A4 (axisym.), with the same input parameters. The PS4 simulation indicates a slope failure at 17 h, the A4 simulation at about 24 h, with the slope failing in the field at about 25 h. If the initial suction is increased by 2.5 kPa, the PS5 (plane strain) also captures the failure time. This small difference between plane strain and axisymmetric formulations is because in the axisymmetric simulation the rainfall infiltration is supposed to be radial, thus the water seepage inside the slope is slightly less than in plane strain condition.

It is found that an increased initial suction in the slope delays the whole progressive failure and reduces the landslide runout. As expected, an increasing friction angle of the kaolinitic layer (*PS1* vs *PS3*) also delays the slope failure, which occurs progressively instead of being abrupt, and also the final landslide runout is reduced. Instead, the larger is the suction reduction parameter (a), the greater is the amount of soil displaced during the landslide process, the shorter are the simulated failure times (e.g. *A4* vs *A1*), and smaller is the runout distance. Finally, the feature of the road influences exclusively the time of second failure and moderately the landslide runout. The field observations are well captured for: $s_0 = 50 - 52.5\ kPa$, $\frac{\tan(\varphi_{kaolin})}{\tan(\varphi'_b)} = 0.75–1.00$and $\varphi'_{kaolin} = 29°$. These back-analysed values are consistent with both: (*i*) the *LEM* and *FEM* shown in the previous section, and (*ii*) field observation (Fig. 12).

6.2. Numerical results versus field evidence

The best-fit simulations (plane strain and axisymmetric) are discussed here and the soil properties are reported in Table 4. The landslide evolution in the case of PS5 plane-strain simulation is commented on starting from 24 h, until when the slope is stable (Fig. 13a). The soil slides along a newly formed shear band as time goes ahead, and a shallow failure is simulated in good agreement (slightly before) with what reported by Knill (1996), see Fig. 13b. This happens because the heavy rainfall makes the wetting front move downward and forms a perched water table of about 2 m above the kaolinitic layer contact. A deeper failure is highlighted by a new shear band and a retrogressive failure mechanism occurs approximately when the second failure was observed (Fig. 13c).

In axisymmetric conditions (case A1, Fig. 14) the evolution of the cumulative plastic strain, displacements and liquid pressure are similar, and the failure mechanism is practically the same as those reported before. The simulated failure time is slightly delayed and the material deposited (Fig. 14c) is smaller than before, but still consistent with the failure times observed in the field.

The displacement time-trend (Fig. 15a) of two points located along the shallow (points *F1* and *F2*) and deep (points *G1* and *G2*) slip surfaces (Figs. 13-14) provide more insights. At *F1-F2*, the computed displacements suddenly increase, indicating the occurrence of the first small failure, about at the time reported by eyewitnesses. At *G1-G2*, the displacements grow suddenly after about 20 min (as observed in the field), indicating that the second major failure occurs. In the plane-strain simulations, the two failures are simulated slightly before than in the axisymmetric ones.

The computed mean effective stresses decrease much when either the first (F1-F2 points) or the second failure (G1-G2 points) occurs. After failure, the mean effective stress slightly increases due to soil consolidation. This plot also helps better understand the progressive failure mechanism of the landslide. In fact, while the F1-F2 points located in the shallow slip surface are characterized by a sudden stress decrease

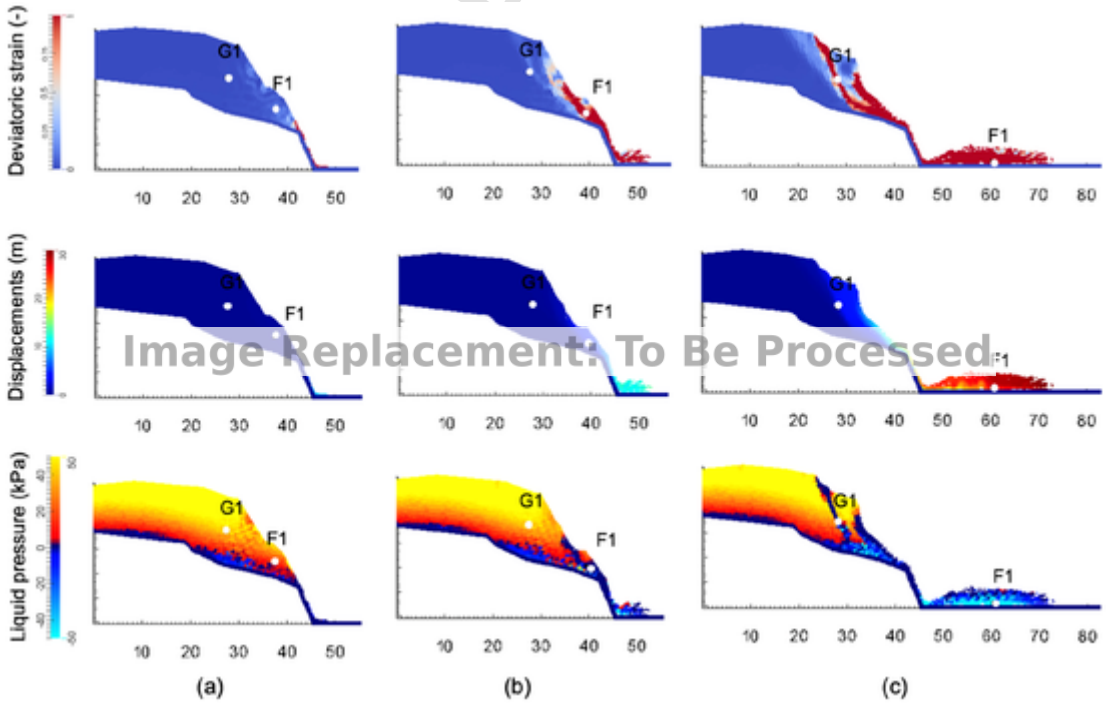

Fig. 13. Trend of deviatoric strain, velocity and displacements computed in plane strain condition and for an initial suction of 50 kPa: (a) $t = 24$ h; (b) $t = 24.44$ h (first failure) and (c) $t = 24.89$ h (second failure).

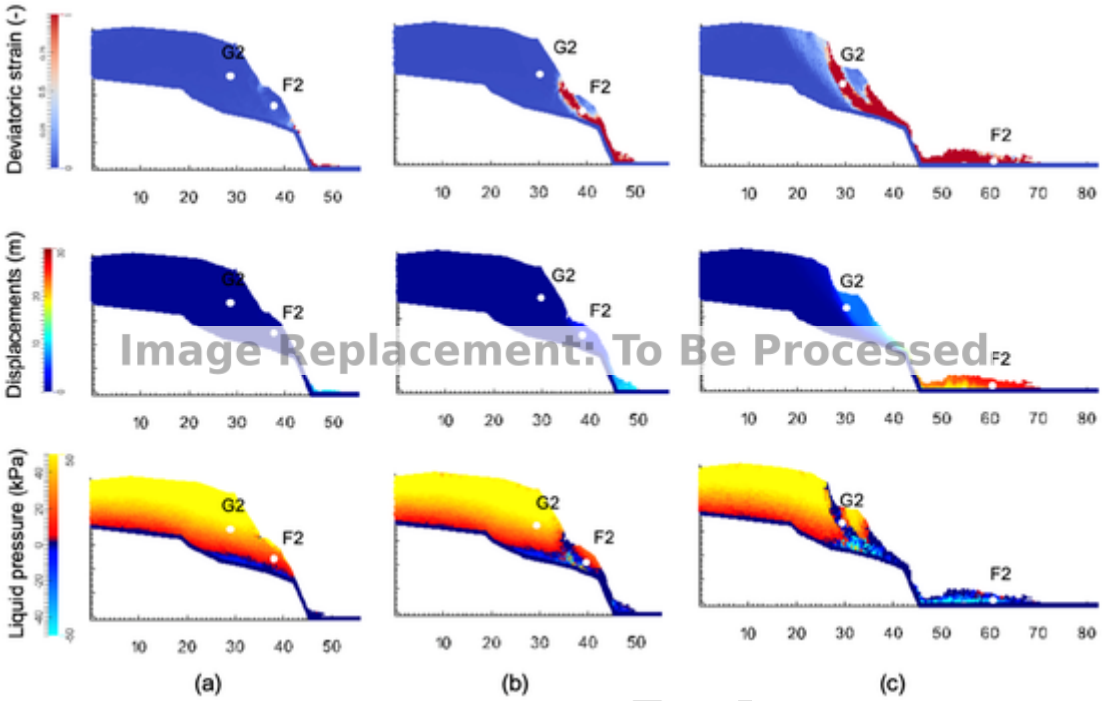

Fig. 14. Trend of deviatoric strain, velocity and displacements computed in axisymmetric condition and for an initial suction of 50 kPa: (a) t = 24 h; (b) t = 24.63 h (first failure) and (c) t = 25.17 h (second failure).

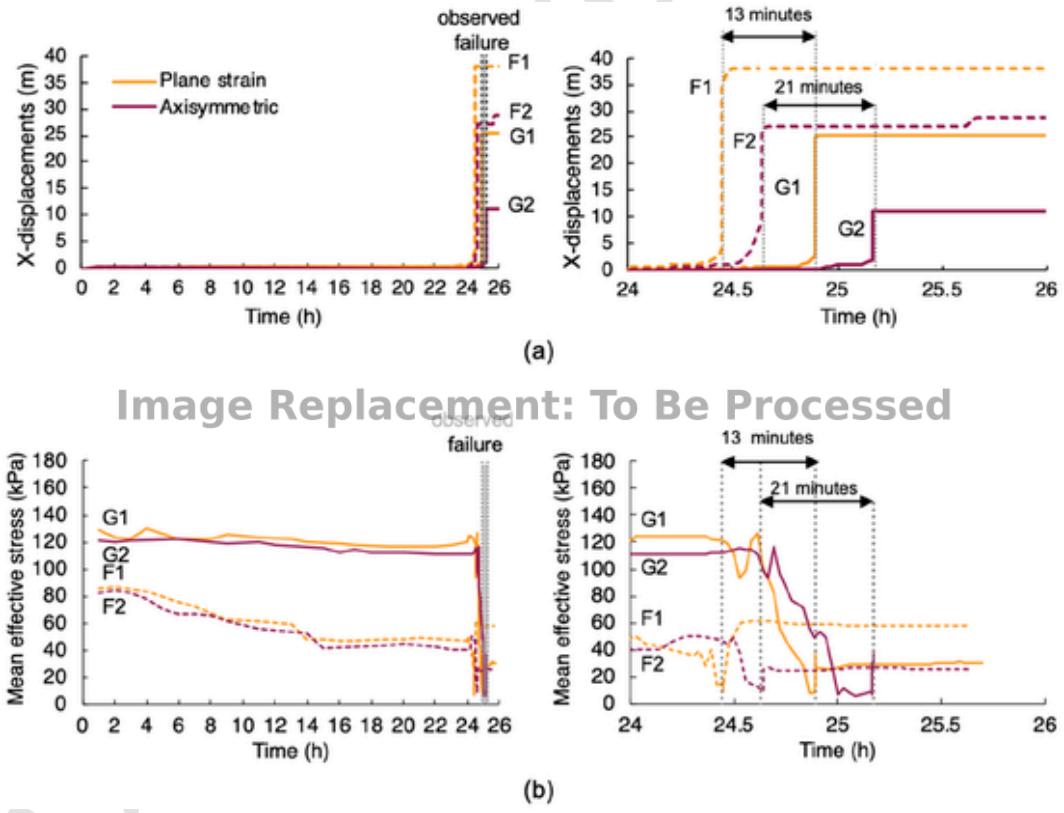

Fig. 15. Temporal trend of the horizontal displacements (a) and mean effective stress (b) inside two reference points in both plane strain and axisymmetric assumptions.

due to the first slope failure, the stress values in the G1-G2 points are still high and drop to zero during the second failure.

Plotting the computed stress paths at these control points (Fig. 16) is also of interest. The most relevant insights are that: (*i*) failure is always

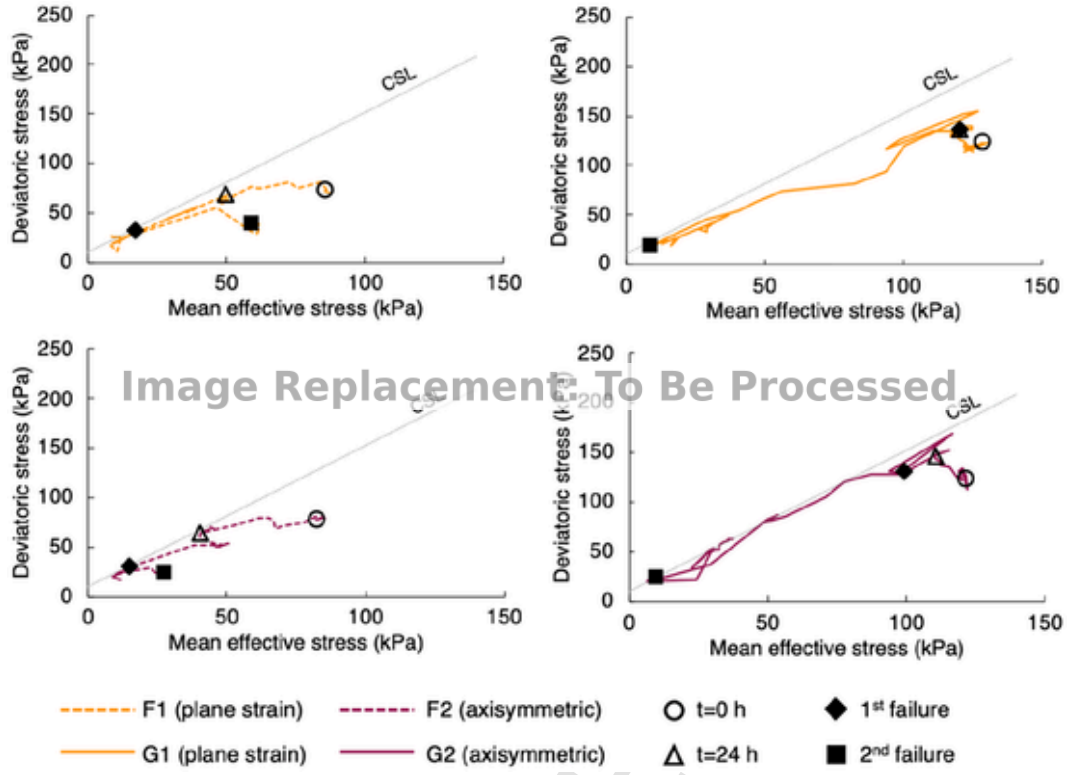

Fig. 16. Stress paths inside the two reference points in both plane strain and axisymmetric assumptions.

reached at low stress state, i.e. in the lower left corner of the graph; (*ii*) when the F-points (shallow slip surface) reach the Critical State Line (*CSL*), the G-points (deep slip surface) are still at high stress levels; (*iii*) the stress paths calculated in plane strain and axisymmetric conditions are similar.

The back-analysed values of the initial suction and the basal friction angle at contact surfaces also allow a good simulation of the observed debris deposition (Fig. 17), highlighting the potential of MPM analysis to reproduce the whole landslide process.

The difference between the plane-strain and axisymmetric assumptions can be better understood looking at the debris deposition. In

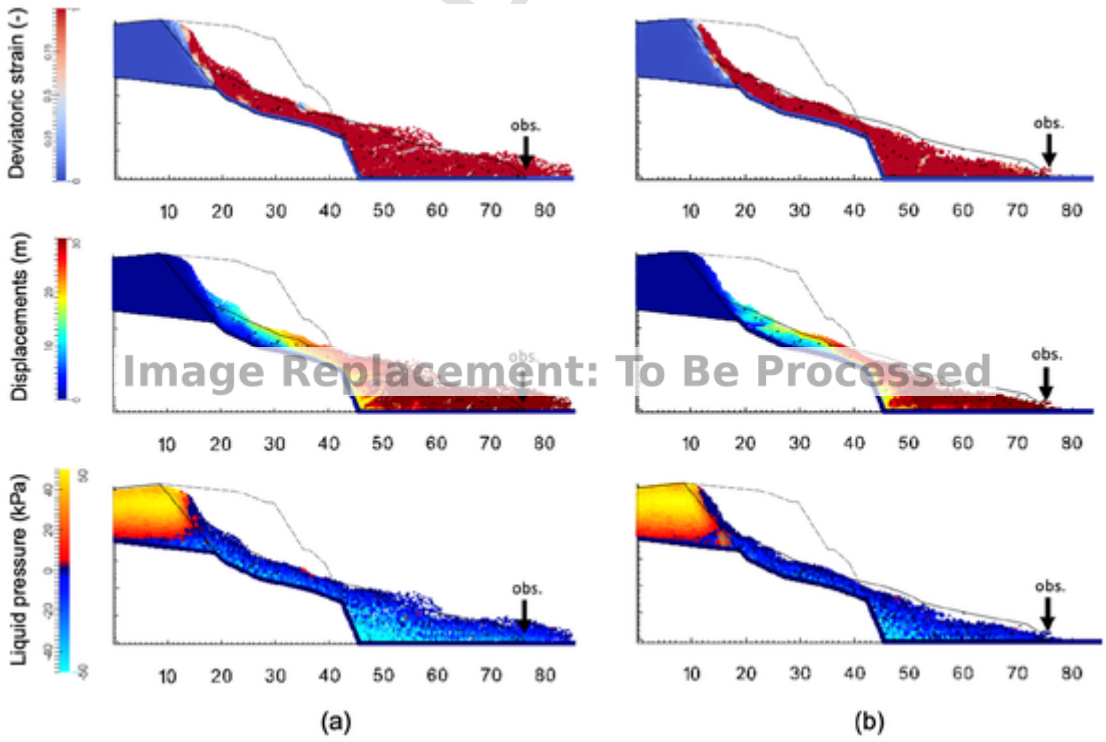

Fig. 17. Observed and simulated debris deposition: (a) plane strain; (b) axisymmetric.

plane-strain condition (Fig. 17a), the calculated final deposition volume per unit width is about 140% of that measured in the field; in the axisymmetric simulation it is equal to 90% (Fig. 17b). Anyway the deformations, displacements and liquid pressure are very similar for both simulations. In fact, the deviatoric strain distribution is everywhere much greater than 1, indicating that the landslide body undergoes large deformations and is completely remoulded. The spatial distribution of the displacements also indicates displacements of the failed mass greater than 30 m from its original position.

Finally, the liquid pressure distribution is also an interesting result to comment more. Inside the landslide body, the liquid pressure: (*i*) increases during the pre-failure rainfall infiltration, (*ii*) is increased more during landslide triggering and propagation, and (*iii*) finally is lowered during deposition. The scar of the landslide remains stable due to the presence of suction. Here, the computed suction is almost unchanged during the whole landslide process, which well explains the field evidence. In previous literature contributions, this portion of the slope has been simply schematized as firm rock (Lee et al., 2019) or practically undeformable soil, i.e. with a cohesion of hundreds of kPa (Liu et al., 2020).

6.3. Discussion

The results achieved highlight the similarities and differences among the models based on: 1) *no-deformation FEM* (also named *uncoupled seepage FEM* in the literature), 2) *small-deformation FEM* (i.e. hydro-mechanical coupled stress-strain FEM), and 3) *large-deformation MPM* (i.e. hydro-mechanical coupled stress-strain *MPM*) in analysing the instability evolution of the slope.

A general agreement among the three computed spatio-temporal distributions of the pore water pressure is observed. This overall agreement validates the independent hypotheses made in each method, and also using independent codes, namely: Seep/W for no-deformation FEM, Plaxis 2D for small-deformation FEM, and Anura 3D for large-deformation *MPM*. For instance, the spatial distributions of pore-water pressure computed at a specific time lapse (t = 18 h), for an initial soil suction uniform along the vertical and equal to 50 kPa, are compared in Fig. 18. Either the unsaturated zone or the water table is very similar in the three models. This is because slope failure is not reached yet and soil deformations are still moderate. However, at specific points, some local differences can be noted in the temporal trend of pore-water pressure computed through the three methods (Fig. 19). The 24-h time trends of the two hydro-mechanical coupled stress-strain models (*small-deformation FEM* and *large-deformation MPM*) are very similar, whereas

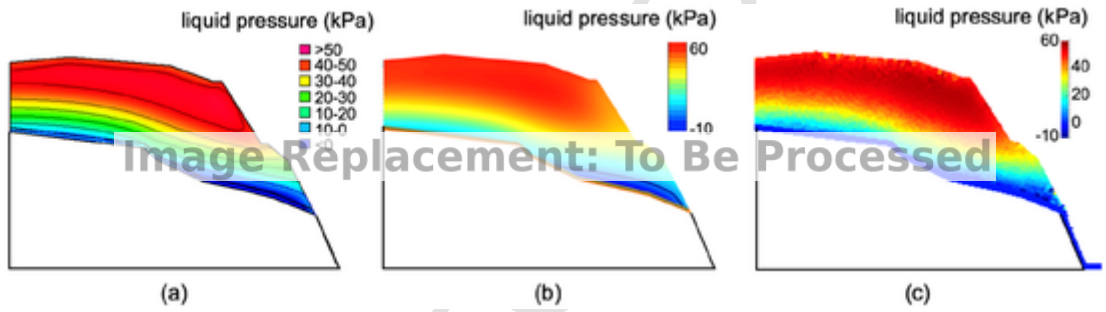

Fig. 18. Pore-water pressure distribution for s_0 = 50 kPa at t = 18 h: (a) no-deformation FEM (b) small-deformation FEM and (c) large-deformation MPM analysis.

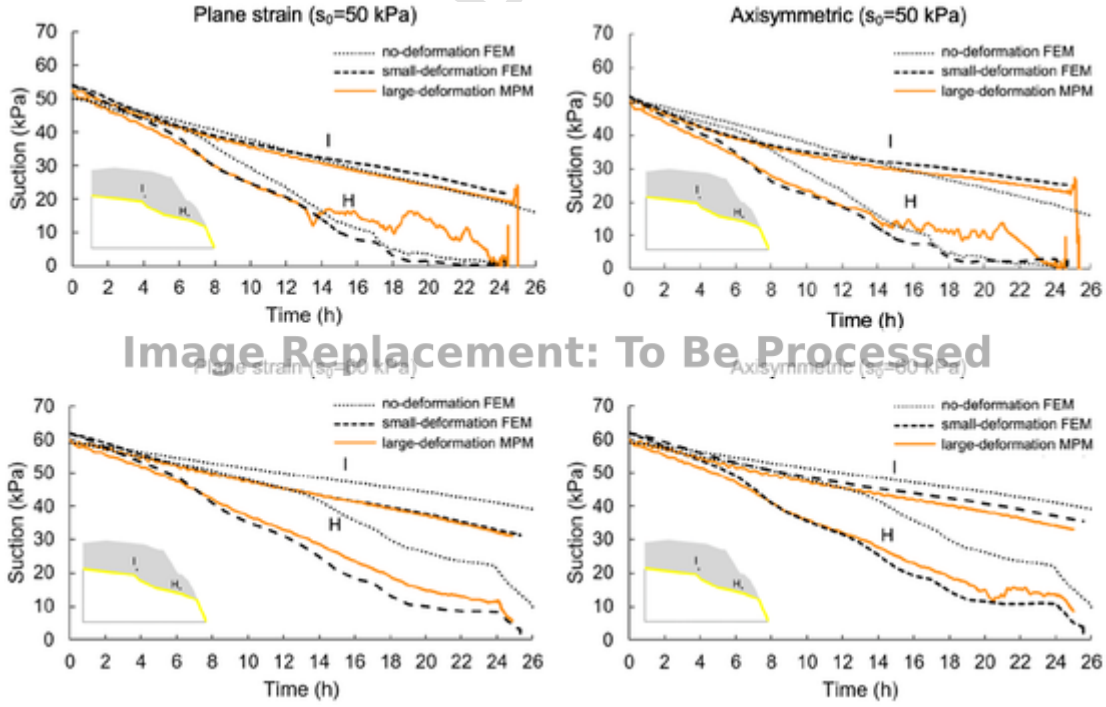

Fig. 19. Comparison among no-deformation FEM analysis, small-deformation FEM analysis and large-deformation MPM analysis in terms of pore-water pressures over time, in axisymmetric and plane strain conditions, for different initial suction.

the *no-deformation FEM* model provides some difference. This is because the model disregards the effect of soil deformations on soil stress and pore-water pressures. Thus, the coupled analysis provides a faster drop of suction compared to the uncoupled model, as expected. In addition, the very fast drop in suction at the rear part of the slope at about 25 h is only captured by the *large-deformation MPM* model.

A good agreement between the *small-deformation FEM* model and the *large-deformation MPM* model is also achieved for the time trends of displacements, computed both in plane strain (Fig. 20a) or axisymmetric (Fig. 20b) conditions until 22–24 h. As the slope failure starts, some differences arise, with the large-deformation *MPM* model being the only one capable of reproducing some sudden accelerations. At a certain stage of the landslide process, the *small-deformation FEM* analysis does not converge while the *large-deformation MPM* model reproduces the whole soil deformation process also including propagation and deposition.

7. Concluding remarks

The paper deals with the simulation of rainfall-induced landslides in an unsaturated slope, by proposing a framework based on a multi-tool approach for modelling. The framework is based on three levels, *no-deformation LEM*, *small-deformation FEM*, *large-deformation MPM*, and it is applied to an international benchmark landslide case (the 1995 Fei Tsui Road landslide in Hong Kong), for its complexity and also for the wide site-specific scientific literature.

A comprehensive series of *LEM*, *FEM* and *MPM* analyses is performed to get insights on various landslide characteristics. The *no-deformation LEM* analysis are used to back-analyse some important unknowns (e.g., initial suction distribution) or uncertain quantities (e.g. critical water table depth) by comparing the observed failures with the safety factor computed at some selected slip surfaces. More comprehensive stress-strain *small-deformation FEM* analyses outline the influence of the initial suction on type and time of slope failure. The more general *large-deformation MPM* (two-phase single-point) modelling simulates the landslide dynamics from failure onset up to soil deposition. The effect and evolution of soil suction in relation to soil shear strain during the whole landslide process is taken into account. In addition, the *MPM* analyses in axisymmetric conditions assess the effects of lateral spreading during the propagation stage.

Based on the achieved results, we observe that fully coupled hydro-mechanical large-deformation models are needed to properly reproduce the complex failure and post-failure mechanisms of rainfall-induced landslides. However, no-deformation *LEM* analyses and small-deformation stress-strain *FEM* analyses provide useful quantitative indications towards the understanding of the failure mechanisms. Moreover, some important quantities that play an important role in the pre-failure and failure stages are properly investigated.

A key issue is the fine-tuning of landslide diagnosis. LEM and FEM analyses are the standard tools for pre-failure and failure stages. However, the modelling of progressive failure, retrogressive landslides, and other cascading effects requires more advanced tools. It is true that enhanced FEM formulations combined with sophisticated soil constitutive equations have much contributed in recent times to the simulation of complex slope instabilities. However, MPM and other large-deformation modelling tools will play a significant role in the future developments about landslide modelling. Thus, while promoting the new emerging numerical tools (among which *MPM* deserves attention), it is still important stressing the value and the indispensable role of more traditional tools in the current engineering practice and research.

Author statement

Sabatino Cuomo, Conceptualization; Writing - original draft

Angela Di Perna, Modelling, Validation; Visualization, Writing - review & editing

Mario Martinelli, conceptualization, methodology, modelling, validation, Software, Supervision, review

Declaration of Competing Interest

The authors declare that they have no known competing financial interests or personal relationships that could have appeared to influence the work reported in this paper.

Acknowledgments

The research was developed within the framework of Industrial Partnership PhD Course (POR Campania FSE 2014/2020). All the MPM simulations were performed using a version of Anura3D developed by Deltares.

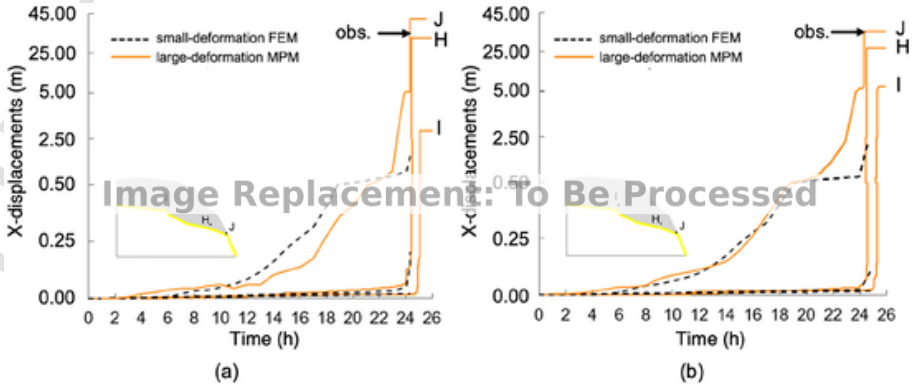

Fig. 20. Comparison among small-deformation FEM and large-deformation MPM results in terms of horizontal displacements for s_0 = 50 kPa: (a) plane strain; (b) axisymmetric.

References

Alonso, E.E., Gens, A., Josa, A., 1990. A constitutive model for partially saturated soils. Géotechnique 40 (3), 405–430.

Bandara, S., Ferrari, A., Laloui, L., 2016. Modelling landslides in unsaturated slopes subjected to rainfall infiltration using material point method. Int. J. Numer. Anal. Methods Geomech. 40 (9), 1358–1380.

Biot, M.A., 1941. General theory of three-dimensional consolidation. J. Appl. Phys. 12 (2), 155–164.

Bishop, A.W., 1954. The use of pore-pressure coefficients in practice. Geotechnique 4 (4), 148–152.

Bishop, A.W., 1955. The use of the slip circle in the stability analysis of slopes. Geotechnique 5 (1), 7–17.

Bishop, A.W., 1959. The principle of effective stress. Teknisk Ukeblad 39, 859–863.

Brinkgreve, R.B.J., Kumarswamy, S., Swolfs, W.M., Waterman, D., Chesaru, A., Bonnier, P.G., 2016. PLAXIS 2016. PLAXIS bv, the Netherlands.

Calvello, M., Cuomo, S., Ghasemi, P., 2017. The role of observations in the inverse analysis of landslide propagation. Comput. Geotech. 92, 11–21.

Cascini, L., Cuomo, S., Pastor, M., Sacco, C., 2013. Modelling the post-failure stage of rainfall-induced landslides of the flow type. Can. Geotech. J. 50 (9), 924–934.

Ceccato, F., Girardi, V., Yerro, A., Simonini, P., 2019. Evaluation of dynamic explicit MPM formulations for unsaturated soils. In: Oñate, M.B., Wriggers, D.R.J.O.P., Zohdi, T. (Eds.), VI International Conference on Particle-based Methods – Fundamentals and Applications PARTICLES 2019 E. pp. 93–102.

Chen, H., Lee, C.F., 2000. Numerical simulation of debris flows. Can. Geotech. J. 37 (1), 146–160.

Chen, X., Zhang, L., Chen, L., Li, X., Liu, D., 2019. Slope stability analysis based on the Coupled Eulerian-Lagrangian finite element method. Bull. Eng. Geol. Environ. 78 (6), 4451–4463.

Chen, X., Zhang, L., Zhang, L., Zhou, Y., Ye, G., Guo, N., 2021. Modelling rainfall-induced landslides from initiation of instability to post-failure. Comput. Geotech. 129, 103877.

Conte, E., Pugliese, L., Troncone, A., 2019. Post-failure stage simulation of a landslide using the material point method. Eng. Geol. 253, 149–159.

Cuomo, S., 2020. Modelling of flowslides and debris avalanches in natural and engineered slopes: a review. Geoenviron. Disast. 7 (1), 1–25.

Cuomo, S., Della Sala, M., 2013. Rainfall-induced infiltration, runoff and failure in steep unsaturated shallow soil deposits. Eng. Geol. 162, 118–127.

Cuomo, S., Prime, N., Iannone, A., Dufour, F., Cascini, L., Darve, F., 2013. Large deformation FEMLIP drained analysis of a vertical cut. Acta Geotech. 8 (2), 125–136.

Cuomo, S., Calvello, M., Villari, V., 2015. Inverse analysis for rheology calibration in SPH analysis of landslide run-out. In: Engineering Geology for Society and Territory-Volume 2. Springer, Cham, pp. 1635–1639.

Cuomo, S., Calvello, M., Ghasemi, P., 2017. Propagation modeling and inverse analysis of a landslide in Hong Kong. In: Workshop on World Landslide Forum. Springer, Cham, pp. 513–521.

Cuomo, S., Di Perna, A., Martinelli, M., 2020. Coupled hydro-mechanical modelling of a 1995 Hong Kong landslide. In: E3S Web of Conferences, vol. 195. EDP Sciences, p. 1028.

Cuomo, S., Di Perna, A., Martinelli, M., 2021. MPM hydro-mechanical modelling of flows impacting rigid walls. Can. Geotech. J.. https://doi.org/10.1139/cgj-2020-0344.

Fick, A., 1855. On liquid diffusion. The London, Edinburgh, and Dublin Philos. Mag. J. Sci. 10, 30–39.

Gan, J.K., Fredlund, D.G., 1996. Shear strength characteristics of two saprolitic soils. Can. Geotech. J. 33 (4), 595–609.

Genuchten, V.M., 1980. A closed-form equation for predicting the hydraulic conductivity of unsaturated soils. Soil Sci. Soc. Am. J. 44 (4), 892–898.

GeoStudio Manual. (2012). Geo-slope international Ltd. Calgary, Alberta, Canada T2P 2Y5.

Ghasemi, P., 2019. Application of Inverse Analysis to Geotechnical Problems, from Soil Behaviour to Large Deformation Modelling. PhD dissertation. University of Salerno. 230 pages.

Gras, J.P., Delenne, J.Y., El Youssoufi, M.S., 2013. Study of capillary interaction between two grains: a new experimental device with suction control. Granul. Matter 15 (1), 49–56.

Hamad, F., 2014. Formulation of a Dynamic Material Point Method and Applications to Soil-Water-Geotextile Systems. Universität Stuttgart Inst. f, Geotechnik.

Haxaire, A., Galavi, V., Brinkgreve, R.B.J., 2011. Fully Coupled Thermo-Hydro-Mechanical Analysis for Unsaturated Soils in Plaxis. Delft University of Technology.

Ho, K.K.S., Lau, J.W.C., 2010. Learning from slope failures to enhance landslide risk management. Q. J. Eng. Geol. Hydrogeol. 43, 33–68.

Kirk, P.A., Campbell, S.D.G., Fletcher, C.J.N., Merriman, R.J., 1997. The significance of primary volcanic fabrics and clay distribution in landslides in Hong Kong. J. Geol. Soc. 154 (6), 1009–1019.

Knill, S.J., 1996. Geo Report No. 188, Hong Kong.

R.C.H. Koo J.S.H. Kwan C. Lam G.R. Goodwin C.E. Choi C.W.W. Ng ... W.K. Pun Back-analysis of geophysical flows using three-dimensional runout model Can. Geotech. J. 55 8 2017 1081 1094

Lee, W.L., Martinelli, M., Shiehi, C.L., 2019. Modelling rainfall-induced landslides with the material point method: the Fei Tsui Road case. In: Proceedings of the XVII ECSMGE-2019. pp. 1–8.

Lei, X., He, S., Chen, X., Wong, H., Wu, L., Liu, E., 2020. A generalized interpolation material point method for modelling coupled seepage-erosion-deformation process within unsaturated soils. Adv. Water Resour. 141, 103578.

Leroueil, S., 2001. Natural slopes and cuts: movement and failure mechanisms. Geotechnique 51 (3), 197–243.

Li, X., Wu, Y., He, S., Su, L., 2016. Application of the material point method to simulate the post-failure runout processes of the Wangjiayan landslide. Eng. Geol. 212, 1–9.

Li, W.C., Deng, G., Cao, W., et al., 2019. Discrete element modeling of the Hongshiyan landslide triggered by the 2014 Ms 6.5 Ludian earthquake in Yunnan, China. Environ. Earth Sci. 78, 520.

Liu, X., Wang, Y., Li, D.Q., 2020. Numerical simulation of the 1995 rainfall-induced Fei Tsui Road landslide in Hong Kong: new insights from hydro-mechanically coupled material point method. Landslides 17 (12), 2755–2775.

Llano-Serna, M.A., Farias, M.M., Pedroso, D.M., 2016. An assessment of the material point method for modelling large scale run-out processes in landslides. Landslides 13, 1057–1066. https://doi.org/10.1007/s10346-015-0664-4.

Martinelli, M., Lee, W.L., Shieh, C.L., Cuomo, S., 2020. Rainfall boundary condition in a multiphase material point method. In: Workshop on World Landslide Forum. Springer, Cham, pp. 303–309.

McMeeking, R.M., Rice, J.R., 1974. Finite Element Formulations for Problems of Large Elastic-Plastic Deformation.

Mualem, Y., 1976. A new model for predicting the hydraulic conductivity of unsaturated porous me-dia. Water Resour. Res. 12 (3), 513–522.

Ng, C.W., Leung, E.H., 2007. Determination of shear-wave velocities and shear moduli of completely decomposed tuff. J. Geotech. Geoenviron. 133 (6), 630–640.

Ng, C.W.W., Wong, H.N., Tse, Y.M., Pappin, J.W., Sun, H.W., Millis, S.W., Leung, A.K., 2011. A field study of stress-dependent soil-water characteristic curves and permeability of a saprolitic slope in Hong Kong. Géotechnique 61 (6), 511.

Nguyen, T.S., Yang, K.H., Ho, C.C., Huang, F.C., 2021. Postfailure characterization of shallow landslides using the material point method. Geofluids 2021.

Nuth, M., Laloui, L., 2008. Effective stress concept in unsaturated soils: clarification and validation of a unified framework. Int. J. Numer. Anal. Methods Geomech. 32 (7), 771–801.

Pastor, M., Haddad, B., Sorbino, G., Cuomo, S., Drempetic, V., 2009. A depth-integrated, coupled SPH model for flow-like landslides and related phenomena. Int. J. Numer. Anal. Methods Geomech. 33 (2), 143–172.

M. Pastor T. Blanc B. Haddad S. Petrone M.S. Morles V. Drempetic ... S. Cuomo Application of a SPH depth-integrated model to landslide run-out analysis Landslides 11 5 2014 793 812

Plaxis, B.V., 2018. PLAXIS 2D Reference Manual. (The Netherlands).

Richards, L.A., 1931. Capillary conduction of liquids through porous mediums. Physics 1 (5), 318–333.

Sanchez, M.E., Pastor, M., Romana, M.G., 2013. Modelling of short runout propagation landslides and debris flows. Georisk: Assessment and Management of Risk for Engineered Systems and Geohazards 7 (4), 250–266.

Scholtès, L., Hicher, P.Y., Nicot, F., Chareyre, B., Darve, F., 2009. On the capillary stress tensor in wet granular materials. Int. J. Numer. Anal. Methods Geomech. 33 (10), 1289–1313.

Soga, K., Alonso, E., Yerro, A., Kumar, K., Bandara, S., 2016. Trends in large-deformation analysis of landslide mass movements with particular emphasis on the material point method. Géotechnique 66 (3), 248–273.

Sulsky, D., Chen, Z., Schreyer, H.L., 1994. A particle method for history-dependent materials. Comput. Methods Appl. Mech. Eng. 118 (1–2), 179–196.

Touma, J., Vauclin, M., 1986. Experimental and numerical analysis of two-phase infiltration in a partially saturated soil. Transp. Porous Media 1 (1), 27–55.

Wang, F., Sassa, K., 2010. Landslide simulation by a geotechnical model combined with a model for apparent friction change. Phys. Chem. Earth Parts A/B/C 35 (3–5), 149–161.

Wang, Y.H., Yan, W.M., 2006. Laboratory studies of two common saprolitic soils in Hong Kong. J. Geotech. Geoenviron. 132 (7), 923–930.

Wang, B., Vardon, P.J., Hicks, M.A., 2018. Rainfall-induced slope collapse with coupled material point method. Eng. Geol. 239, 1–12.

Yerro Colom, A., 2015. MPM Modelling of Landslides in Brittle and Unsaturated Soils. PhD Dissertation. UPC, Spain.

Yerro Colom, A., de Alonso Pérez Agreda, E., Pinyol Puigmartí, N.M., 2015. The material point method for unsaturated soils. Géotechnique 65 (3), 201–217.

Yerro, A., Alonso, E., Pinyol, N., 2016. Modelling large deformation problems in unsaturated soils. In: E3S Web of Conferences, vol. 9. EDP Sciences, p. 8019.

Yerro, A., Soga, K., Bray, J., 2019. Runout evaluation of Oso landslide with the material point method. Can. Geotech. J. 56 (9), 1304–1317.

Yuan, C., Moscariello, M., Cuomo, S., Chareyre, B., 2019. Numerical simulation of wetting-induced collapse in partially saturated granular soils. Granul. Matter 21 (3), 64.

Zhao, C.F., Kruyt, N.P., Millet, O., 2019. Capillary bridges between unequal-sized spherical particles: Rupture distances and capillary forces. Powder Technol. 346, 462–476.

Zhao, L., Liu, X., Mao, J., et al., 2020. Three-dimensional distance potential discrete element method for the numerical simulation of landslides. Landslides 17, 361–377.